

A combined direct numerical simulation–particle image velocimetry study of the turbulent near wake

By S. DONG¹†, G. E. KARNIADAKIS¹‡, A. EKMEKCI²
AND D. ROCKWELL²

¹Division of Applied Mathematics, Brown University, Providence, RI 02912, USA

²Department of Mechanical Engineering, Lehigh University, Bethlehem, PA 18015, USA

(Received 8 March 2005 and in revised form 28 May 2006)

We investigate the near wake of a cylinder at values of Reynolds number corresponding to the onset and development of shear-layer instabilities. By combining quantitative experimental imaging (particle image velocimetry, PIV) and direct numerical simulations at $Re = 3900/4000$ and $10\,000$, we show that the flow structure is notably altered. At higher Reynolds number, the lengths of both the wake bubble and the separating shear layer decrease substantially. Corresponding patterns of velocity fluctuations and Reynolds stress contract towards the base of the cylinder. The elevated values of Reynolds stress at upstream locations in the separated layer indicate earlier onset of shear-layer transition. These features are intimately associated with the details of the shear-layer instability, which leads to small-scale vortices. The simulated signatures of the shear-layer vortices are characterized by a broadband peak at $Re = 3900$ and a broadband high spectral-density ‘plateau’ at $Re = 10\,000$ in the power spectra. The shear-layer frequencies from the present direct numerical simulations study agree well with previous experimentally measured values, and follow the power law suggested by other workers.

1. Introduction

The near-wake of a circular cylinder becomes particularly complex when transition occurs in the separating shear layers. With increasing Reynolds number, the onset of transition moves upstream towards the separation point and, simultaneously, the large-scale Kármán-like vortices are formed closer to the base of the cylinder. These variations of the wake structure have important consequences for both the steady and unsteady loading on the cylinder. In order to provide a perspective on the wake structure of interest herein, related experimental and numerical investigations are reviewed in the sections that follow.

Experimental investigations

Experimental insight into the phenomena of instability and transition in the near-wake, along with overviews of related investigations, are given by Gerrard (1967), Roshko & Fiszdon (1969), McCroskey (1977), Unal & Rockwell (1988),

† Present address: Center for Computational and Applied Mathematics, Department of Mathematics, Purdue University, West Lafayette, IN47907, USA.

‡ Author to whom correspondence should be addressed: gk@dam.brown.edu

Zdravkovich (1990), Szepessy & Bearman (1992), Lin, Towfighi & Rockwell (1995), Williamson (1996) and Norberg (2003). Detailed insight into the structure as well as the predominant frequency of the shear-layer instability/transition is reviewed by Williamson (1996), originating with the studies of Bloor (1964) and Gerrard (1967). The works of Gerrard (1978), Wei & Smith (1986), Filler, Marston & Mih (1991), Roshko (1993), Sheridan *et al.* (1993), Lin *et al.* (1995), Williamson (1996), Chyu & Rockwell (1996), Prasad & Williamson (1997), Norberg (1998) and Brede (2004) characterize various features of these small-scale structures.

In addition to the time-averaged characteristics that are influenced by the existence of small-scale structures, Noca, Park & Gharib (1998) provide summaries of various interpretations of the formation length as a function of Reynolds number and show quantitative images of the near-wake structure at $Re = 1260$. Saelim (2003) and Ekmekci (2006) have related the transitional phenomena in the separating shear layer to variations of patterns of Reynolds stress, entrainment velocity and onset of large-scale vortex formation in the near wake over the Reynolds number range $Re = 1000$ to 10 000. At $Re = 10\,000$, pronounced small-scale concentrations of vorticity are evident in the shear layer shortly after separation and, correspondingly, the large-scale Kármán-like vortices are formed close to the base of the cylinder. This state of the shear layer contrasts with the structure at substantially lower values of Reynolds number, for which the onset of the first small-scale concentration of vorticity occurs well downstream of separation, if at all. Based on the experimental investigations cited in the foregoing, the patterns of the near wake at $Re = 4000$ and 10 000 are representative of transition phenomena in the separating shear layers, and therefore are selected for the experimental–numerical comparisons of the present investigation.

Numerical simulations

Simulation of the near-wake structure has been undertaken at various values of Reynolds number using several approaches. Herein, we focus on investigations at values of Reynolds number for which transition most probably occurred in the separating shear layers. The Reynolds number $Re = 3900$ has been the most extensively numerically investigated one in the transition range. Beaudan & Moin (1994), Mittal & Moin (1997), Kravchenko & Moin (2000) performed the first large-eddy simulations (LES) at this Reynolds number. They demonstrate that upwinding schemes are overly dissipative for cylinder flow turbulence simulations. The mean flow and Reynolds stress from these computations are in good agreement with the experimental data. However, in the vicinity of the cylinder, all three simulations converge to a mean velocity profile different from the experimental result. The numerical and modelling aspects that affect the quality of LES are further investigated by the following studies at this Reynolds number. Breuer (1998) has further confirmed that dissipative methods are inferior to central differencing schemes in terms of agreement with experimental data and the accuracy in predicting physical quantities such as the base pressure coefficients. In light of the relatively short statistics accumulation time in some LES studies, Franke & Frank (2002) examine the effect of the averaging time on the accuracy of statistical quantities, and observe a notable influence on the values of base pressure coefficients and the re-circulation bubble length. Resolving the inertial range properly is another issue in LES as the upwinding scheme coupled with dynamic subgrid scale (SGS) models lacks full control over the aliasing when the cutoff falls below the lower limit of the inertial range (Jordan 2003). The only direct numerical simulation (DNS) was performed by Ma, Karamanos & Karniadakis (2000) for the cylinder flow at $Re = 3900$ using a spectral element scheme

on unstructured meshes. The mean flow and energy spectra are in good agreement with the experimental data in the near wake as well as far downstream. In particular, the mean velocity profiles agree well with the experiment in the vicinity of the cylinder.

The cylinder flow at higher Reynolds numbers in the transition range has been considered by several other LES studies. Jordan (2002) studied the shear-layer instability at Reynolds number $Re = 8000$ employing an LES scheme with second-order upwind finite differencing coupled with a dynamic SGS model in curvilinear systems. A number of flow quantities have been calculated correctly, and the shear-layer frequency has been captured reasonably well. However, the lift coefficient from the computation is much lower than the experimental values (Norberg 2003). In addition, only a short time history (about 25 convective units) is collected, which may influence the power spectra and the accuracy of the Strouhal frequency. Kalro & Tezduyar (1997) conducted an LES study at $Re = 10\,000$, based on a stabilized finite-element formulation and a Smagorinsky subgrid model. The drag coefficient and Strouhal number are predicted reasonably well. However, no grid refinement was conducted and no statistics were reported. Breuer (2000) investigated the cylinder flow at $Re = 140\,000$ in order to evaluate the applicability of LES to high-Reynolds-number flows. The predicted integral parameters and the mean velocity profiles are in reasonable agreement with experimental measurement; however, the grid refinement does not lead to improved results in terms of agreement with the experimental data.

Two-dimensional simulation has been known to tend to over-predict the fluid forces on the cylinder owing to intrinsic three-dimensional effects (Batcho & Karniadakis 1991; Mittal & Balachandar 1995), which is exemplified by several two-dimensional studies at Reynolds numbers in the transitional range (Braza, Chassaing & Ha Minh 1990; Mittal & Kumar 2001). However, it has predicted the shear-layer frequency surprisingly well. Braza *et al.* (1990) simulated the cylinder flow at Reynolds numbers $Re = 2000$ – $10\,000$ by solving the two-dimensional Navier–Stokes equations with a finite-volume method. Although the lift coefficients are highly over-predicted, the shear-layer frequencies from the computations are in quite good agreement with the experimental results.

Objective

In this paper, we investigate the Reynolds-number effects on the cylinder wake statistics and the shear-layer instabilities in the transitional range. To this purpose, we have conducted high-resolution particle image velocimetry (PIV) experimental measurements of the cylinder wake at Reynolds numbers $Re = 4000$ and $10\,000$, and performed three-dimensional direct numerical simulations at $Re = 3900$ and $10\,000$. We focus on the comparison between experimental and simulation results to elucidate how the Reynolds number affects the distributions of a number of statistical quantities such as the mean vorticity, Reynolds stress, and r.m.s. fluctuations, and how the variation of Reynolds number affects the flow spectra and frequencies of the shear layer.

2. Experimental and numerical techniques

Experiments were undertaken in a large-scale free-surface water channel having a length of 5435 mm, a depth of 594 mm and a width of 613 mm. Upstream of this test section, the flow passed through a settling chamber and an extensive flow-conditioning section, and then finally through a 3:1 contraction, which yielded a very low level free-stream turbulence intensity of less than 0.1%. Small-amplitude

perturbations that potentially can arise at locations downstream of the cylinder, and may propagate upstream, were isolated from the inflow configuration and test section via a honeycomb damping system. A system of 1 μm water filters ensured high water purity during water replacement between experimental runs; this process optimized the quality of quantitative imaging of reflective particles seeded in the water. Moreover, the water temperature was controlled during the replacement process. Additional characteristics of this facility are described in Fu & Rockwell (2005).

The diameter of the cylinder (denoted by D) was 50.8 mm, and the nominal free-stream velocity of 197 mm s^{-1} corresponded to a Reynolds number of $Re = 10\,000$ based on cylinder diameter. The cylinder was bounded by an end-plate at its bottom boundary and the free surface at its top boundary. The end-plate was rectangular. It spanned the width of the channel, had a streamwise length of $7.5D$, and was bevelled at its leading edge with an angle of 23.6° . The distance between the cylinder axis and the leading edge was $3D$. The effective aspect ratio of the cylinder was 8.78. Norberg (1994) has shown experimentally that as the cylinder aspect ratio increases from 7.5 to 80, the base pressure coefficient increases from 0.81 to 0.87 at $Re = 4000$ (base pressure coefficient is 0.88 from present DNS at $Re = 3900$ for a U-type solution), and decreases from 1.16 to 1.10 at $Re = 10\,000$ (base pressure coefficient is 1.129 from present DNS at $Re = 10\,000$). High-image-density particle-image velocimetry was employed to determine the instantaneous, time-averaged structure of the near-wake. A dual-pulsed YAG laser system, operating at 120 mJ pulse^{-1} , successively illuminated hollow plastic spheres of 14 μm diameter.

To determine the degree of two-dimensionality of the near wake, a vertical laser sheet was aligned coincident with the plane of symmetry of the cylinder, and imaging was performed using the same approach and post-processing as for the plane orthogonal to the cylinder axis. Images of the velocity field, with a spatial resolution of $0.05D$, led to patterns of averaged streamline topology with a well-defined bifurcation line along the span, and contours of constant streamwise velocity with a sharply defined demarcation line located between positive and negative contours, and extending along the span. The latter is particularly suitable for quantitatively defining the degree of spanwise two-dimensionality. Let $\langle L_u/D \rangle$ represent the dimensionless time-averaged distance from the base of the cylinder to the demarcation line. It was evaluated over a spanwise distance of $3D$ beneath and $3.47D$ above the location of the horizontal laser sheet, i.e. a total span of $6.47D$. (The midspan of the submerged portion of the cylinder was a distance of $1.39D$ from the location of the plane of the laser sheet.) Let $\langle L_u/D \rangle_{avg}$ denote the spatially averaged value of $\langle L_u/D \rangle$, and $\langle L_u/D \rangle_{rms}$ denote the root-mean-square deviation from $\langle L_u/D \rangle_{avg}$. At $Re = 4000$ and $10\,000$, $\langle L_u/D \rangle_{rms}/\langle L_u/D \rangle_{avg} = 0.031$ and 0.026 , respectively. The averaged values were $\langle L_u/D \rangle_{avg} = 1.52D$ for $Re = 4000$ and $\langle L_u/D \rangle_{avg} = 0.85D$ for $Re = 10\,000$.

For the sectional (horizontal plane) imaging of the flow structure, the laser sheet was at an elevation of three cylinder diameters from the surface of the end-plate. The field of view in the physical plane of the laser sheet was $96.8 \text{ mm} \times 98.8 \text{ mm}$. Existence of a narrow band of reflected laser light, in the region below the lower shear layer of the cylinder, provided unacceptable illumination of the particle images passing through that region, and therefore the correlation technique for evaluation of velocity could not be accurately implemented. The domain of predominant distortion due to this reflection is defined by the blank region in the patterns of figures 6(a) and 7(a) (PIV results). A frame-to-frame cross-correlation technique was employed to determine patterns of velocity vectors. Each instantaneous vector field of approximately 2550 velocity vectors was generated by employing an interrogation window of $32 \text{ pixels} \times 32$

pixels, with a 50 % overlap. These instantaneous patterns of velocity were then used to determine the patterns of streamwise and transverse (crossflow) velocity components, mean velocities, as well as patterns of root-mean-square velocity. Finally, contours of Reynolds stress were determined. To obtain the averaged quantities, a total of 600 instantaneous images were employed.

We performed three-dimensional direct numerical simulations of the cylinder flow by solving the incompressible Navier–Stokes equations employing a Fourier spectral expansion in the homogeneous direction and a spectral element approach (Karniadakis & Sherwin 2005) in the streamwise and crossflow directions. For time integration, a stiffly stable pressure correction-type scheme is employed with a third-order accuracy in time (Karniadakis, Israeli & Orszag 1991). A uniform inflow is prescribed at the inlet. No-slip conditions are applied to the cylinder surface. The Neumann boundary condition is used at the outflow, and the periodic boundary condition is applied in the crossflow direction. We have simulated the turbulent cylinder wake at two Reynolds numbers, $Re = 3900$ and $10\,000$, based on the free-stream velocity and the cylinder diameter. For Reynolds number $Re = 3900$, the computational domain extends from $-15D$ at the inlet to $25D$ at the outlet, and from $-9D$ to $9D$ in the crossflow direction. Extensive grid refinement tests have been conducted; see Ma *et al.* (2000) for details and Appendix B for additional tests on spanwise resolutions. In the present study, we employ an unstructured mesh of 902 spectral elements in the streamwise-crossflow planes, with eighth-order Jacobi polynomial expansions on each element. In the homogeneous spanwise direction, we employ 32 to 96 Fourier modes (or 64 to 192 grid points) on a domain with the spanwise dimension of $L_z/D = 1.5\pi$, as well as 64 Fourier modes (or 128 grid points) on a domain with the spanwise dimension of $L_z/D = \pi$. These parameters lead to grid spacings near the cylinder surface of 0.32 in the radial direction, 0.68 in the azimuthal direction, and 2.17 in the spanwise direction in viscous wall units based on the friction velocity at the top tip of the cylinder, $(x, y) = (0, 0.5D)$. For Reynolds number $Re = 10\,000$, the computational domain extends from $-20D$ at the inlet to $50D$ at the outlet, and from $-20D$ to $20D$ in the crossflow direction. The spanwise dimension of the domain is chosen to be $L_z/D = \pi$. Extensive grid refinement tests have been performed at $Re = 10\,000$; see Appendix A for details. In the present study, we employ two unstructured spectral meshes in each streamwise-crossflow plane: a coarse mesh with 6272 triangular elements and a refined mesh with 9272 triangular elements, with fifth-order Jacobi polynomial expansions on each element. In the homogeneous direction, we employ 64 Fourier modes (or 128 grid points). These parameters lead to grid spacings near the cylinder surface of 0.31 in the radial direction, 0.65 in the azimuthal direction and 5.31 in the spanwise direction in viscous wall units based on the friction velocity at the top tip of the cylinder. We have performed long-time simulations of flows at both Reynolds numbers. After the initial transient convects away, the statistical quantities are accumulated until convergence, which amounts to about 200 to 250 convective time units (D/U_0) or about 40 to 50 shedding cycles.

3. Flow statistics

Figure 1 compares the normalized mean spanwise vorticity $\bar{\omega}_z D/U_0$ between experiment and simulation. We plot mean vorticity contours at $Re = 4000$ for PIV and at $Re = 3900$ for DNS on the same contour levels. The field of view of the flow domain in this and subsequent plots are also the same from both experiment and simulation, with $0.148 < x/D < 2.053$ and $-0.968 < y/D < 0.976$ for $Re = 3900/4000$,

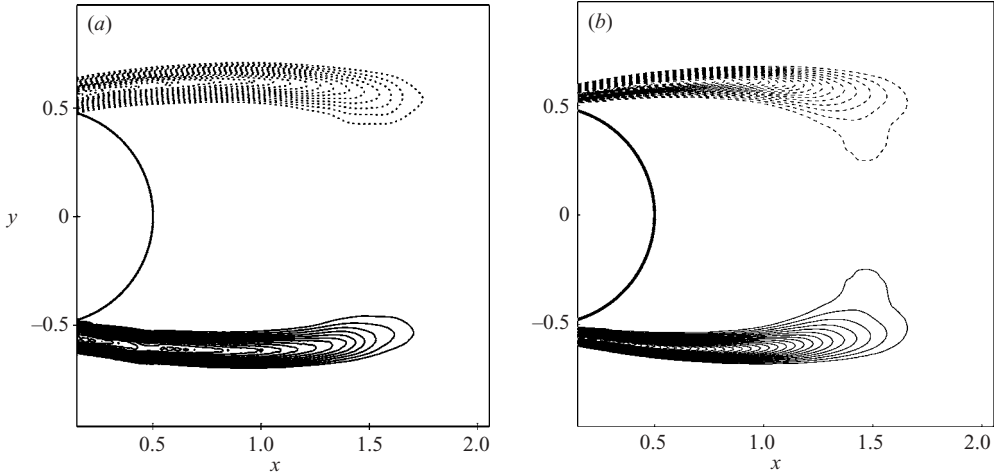


FIGURE 1. Contours of normalized mean spanwise vorticity: (a) PIV at $Re = 4000$; (b) DNS at $Re = 3900$. In both plots, $|\bar{\omega}_z D/U_0|_{min} = 2.58$ and $|\Delta\bar{\omega}_z D/U_0| = 0.64$.

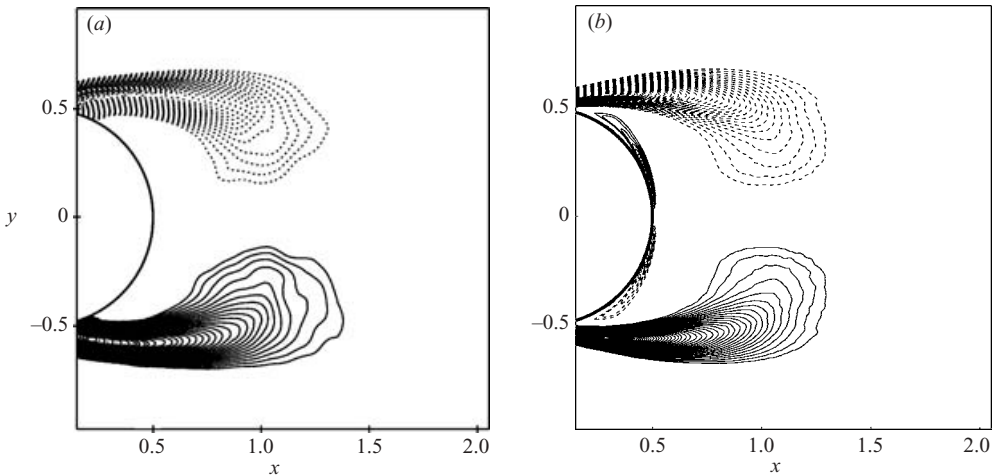


FIGURE 2. Contours of normalized mean spanwise vorticity at $Re = 10000$: (a) PIV; (b) DNS. In both plots, $|\bar{\omega}_z D/U_0|_{min} = 1.61$ and $|\Delta\bar{\omega}_z D/U_0| = 0.32$.

and $0.148 < x/D < 2.053$ and $-0.978 < y/D < 0.966$ for $Re = 10000$. The patterns of the mean vorticity from the simulation and experiment are very similar. The vorticity distributions exhibit an absence of significant vorticity levels in the cylinder base region at this Reynolds number, a feature first noted by Lin *et al.* (1995). Furthermore, the two shear layers extend from the centre of the cylinder to $1.65D$ and $1.74D$, respectively, in the simulation and experiment.

For comparison with $Re = 3900/4000$, in figure 2 we plot contours of the normalized mean spanwise vorticity at Reynolds number $Re = 10000$ from the experiment and the simulation. Experimental and DNS results are again plotted with the same contour levels. Remarkably similar patterns of vorticity distributions are again observed for both experiment and simulation. DNS shows notable vorticity levels in the vicinity of the cylinder surface above and below the cylinder base at $Re = 10000$, a feature not detectable in the experimental result. We suspect that the absence is due to the

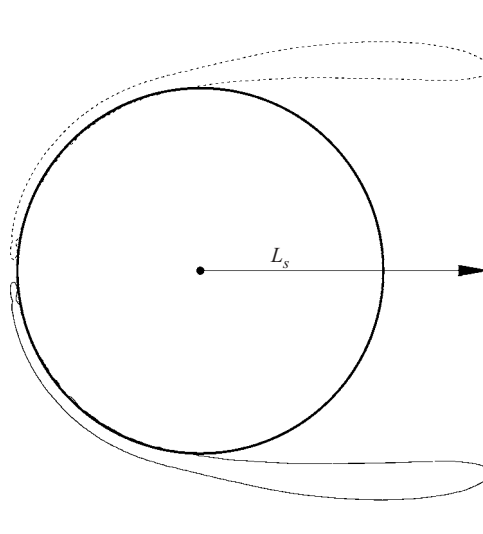


FIGURE 3. Illustration of effective shear layer length L_s . The mean spanwise vorticity contour in the plot is at a level of 8% of the maximum mean vorticity magnitude along a vertical line crossing the cylinder axis, $x=0.0$.

limited resolution of PIV on the cylinder surface. Furthermore, it should be noted that the minimum vorticity level employed in the PIV image corresponds to the value above which the vorticity magnitude was free of PIV processing noise. At $Re = 10\,000$ the shear layer is significantly shorter than at $Re = 3900/4000$, extending downstream of the centre of the cylinder a distance of $1.29D$ and $1.35D$, respectively, for the simulation and experiment. On the other hand, the tip of this averaged vorticity layer is significantly thicker than that at $Re = 3900/4000$; that is, it bulges inward toward the centreline. The differences in vorticity structure shown here between $Re = 3900/4000$ and $10\,000$ are consistent with previous observations, which indicate that the region of transition and von Kármán vortex shedding moves towards the cylinder with increasing Reynolds number (Linke 1931; Bloor 1964; Wei & Smith 1986; Kourta *et al.* 1987; Unal & Rockwell 1988; Lin *et al.* 1995; Prasad & Williamson 1997; Noca *et al.* 1998; Norberg 1998).

To provide a quantitative measure of the difference in the shear layer between these two Reynolds numbers, we define an effective shear-layer length, L_s , as the downstream location of the tip of a mean spanwise vorticity contour line at the level of 8% of a reference vorticity, namely $\bar{\omega}_z/\bar{\omega}_m = 0.08$, where the reference vorticity $\bar{\omega}_m$ is the maximum mean spanwise vorticity magnitude along the vertical line crossing the cylinder axis, $x=0.0$ (figure 3). We computed the effective shear-layer lengths in DNS for $Re = 3900$ and $10\,000$, and present the results in table 1. At $Re = 3900$, the shear-layer length of the ‘U’-type wake is about 11–16% longer than that of the ‘V’-type wake (see Ma *et al.* 2000 for detailed discussion of these two types of wake). In the present study, we observe a ‘U’-type near-wake in the case with a spanwise dimension $L_z/D = \pi$ (and 64 Fourier modes in the spanwise direction), and a ‘V’-type near-wake in the case with a spanwise dimension $L_z/D = 1.5\pi$ (with 32, 64 and 96 Fourier modes in the spanwise direction). DNS results shown in figure 1 and subsequent plots for $Re = 3900$ are with the ‘U’-type near-wake. At $Re = 10\,000$, the shear-layer length from the high-resolution mesh (9272 elements) differs from

		L_z/D	N_z	K	L_s/D
$Re = 3900$	'U'-type	π	128	902	1.59
	'V'-type	1.5π	64	902	1.43
	'V'-type	1.5π	128	902	1.37
	'V'-type	1.5π	192	902	1.41
$Re = 10\,000$		π	128	9272	1.03
		π	128	6272	0.90

TABLE 1. Effective shear-layer length from DNS for Reynolds numbers $Re = 3900$ and $10\,000$. L_z is the spanwise dimension of flow domain; N_z is the number of grid points in the z -direction; K denotes the number of spectral elements in (x, y) -planes. L_s denotes the effective shear-layer length; see text and figure 3 for its definition.

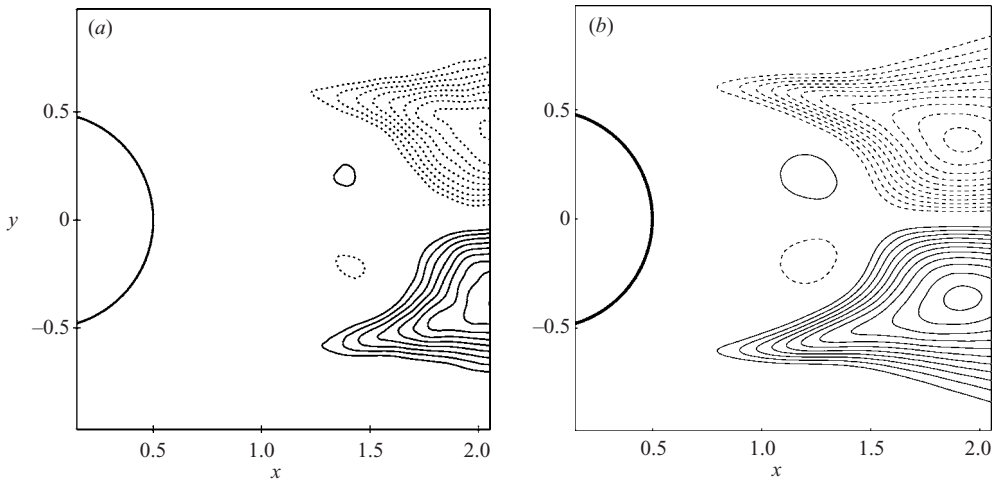


FIGURE 4. Contours of normalized Reynolds stress: (a) PIV at $Re = 4000$; (b) DNS at $Re = 3900$. In both plots, $|\langle u'v' \rangle / U_0^2|_{min} = 0.03$ and $|\Delta \langle u'v' \rangle / U_0^2| = 0.01$.

that of the low-resolution mesh (6272 elements) by about 13%. DNS results shown in figure 2 and subsequent plots for $Re = 10\,000$ are based on the high-resolution mesh. Comparison of the 'U'-type wake at $Re = 3900$ and high-resolution result at $Re = 10\,000$ indicates that the shear layer is about 30% shorter at the higher Reynolds number than at the lower one.

In figure 4, we plot contours of the normalized Reynolds stress $\langle u'v' \rangle / U_0^2$ at $Re = 3900/4000$, where u' and v' are streamwise and crossflow root mean square (r.m.s.) velocities, respectively. Four distinct 'lobes' are evident in both the patterns, two small clusters in the front and two large ones further downstream. They are anti-symmetric with respect to the centreline. The Reynolds stress exhibits an absence of significant levels in the base region and in the shear layer close to the cylinder surface, indicating either small magnitudes of the fluctuations and/or the lack of significant correlation between streamwise and crossflow fluctuations in the very near wake of the cylinder. The locations of the dominant Reynolds stress peaks are at $x/D = 1.90$ and 2.05 , respectively, for simulation and experiment. These dominant peaks of the Reynolds stress distribution have levels of 0.14 and 0.11 , respectively, for simulation and experiment. Note, however, that the 'tails' of the patterns of Reynolds

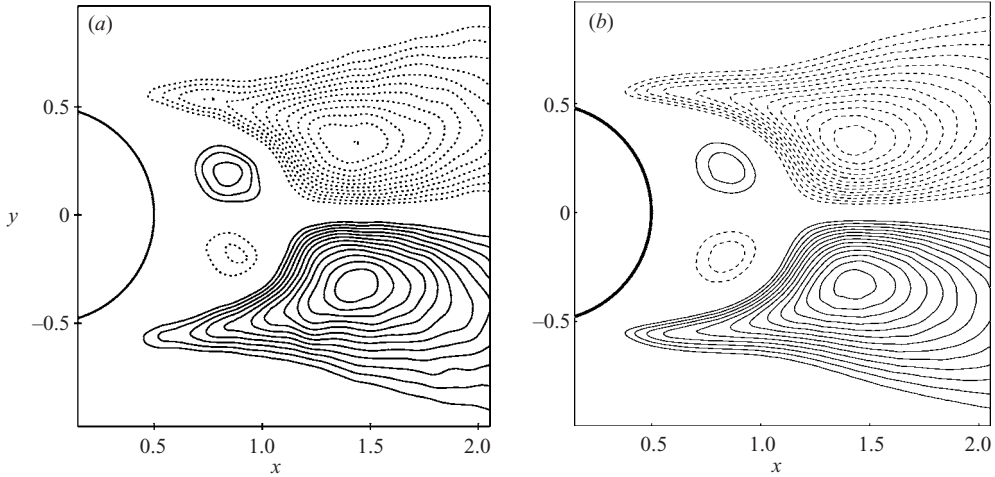


FIGURE 5. Contours of normalized Reynolds stress at $Re = 10000$: (a) PIV; (b) DNS. In both plots, $|\langle u'v' \rangle / U_0^2|_{min} = 0.03$ and $|\Delta \langle u'v' \rangle / U_0^2| = 0.01$.

stress, which extend upstream, are longer for the simulation than for experiment. These tails coincide with the tip regions of the shear layers (see figure 1), and the notable Reynolds stress levels in these regions result from the shear-layer instability and the rolling-up of shear-layer vortices. The longer ‘tail’ in simulations may result from an earlier onset of transition.

Figure 5 shows comparison of the normalized Reynolds stress at $Re = 10000$ for experiment and simulation. The overall form of these patterns is similar to those at $Re = 3900/4000$ given in figure 4. Low-level clusters of Reynolds stress are again observed at locations upstream of the dominant clusters. However, the entire pattern of Reynolds stress has moved a substantial distance upstream, relative to the patterns at $Re = 3900/4000$. The location of the peak Reynolds stress is now at $x/D = 1.4$; it has levels of 0.15 and 0.14, respectively, for simulation and experiment. Moreover, the small-scale clusters of Reynolds stress are located immediately downstream of the cylinder base. Particularly important are the upstream extensions of the large-scale clusters, along the locus of the separating shear layer towards the point of separation on the surface of the cylinder. These elongated regions are indicative of the early transition of the separated layer. For both experiments and simulation, the tip of this upstream extended region reaches upstream of the base of the cylinder.

We next examine the mean flow characteristics in the cylinder wake. Figure 6 compares the distribution of the normalized mean streamwise velocity u/U_0 from the experiment at $Re = 4000$ (figure 6a) and from the simulation at $Re = 3900$ (figure 6b). These patterns of mean streamwise velocity, show a well-defined bubble of negative velocity, that is, reverse flow. The location and the magnitude of the minimum are close in value for simulation and experiment. For the PIV images, the maximum magnitude of the negative velocity is $u/U_0 = 0.252$ and 0.228 for $Re = 4000$ and $Re = 10000$, respectively, in simulations, they are 0.291 and 0.249 for these two Reynolds numbers. Norberg (1998) obtained these values via laser-Doppler velocimetry (LDV) measurements. From interpolation of his results, we obtain a rounded value of $u/U_0 = 0.44$ at $Re = 4000$; at $Re = 10000$, the un-interpolated value is $u/U_0 = 0.38$. The streamwise extent of the bubble can be evaluated along its centreline. The lengths of the bubbles, i.e. the distance from the base of the cylinder to the location at zero

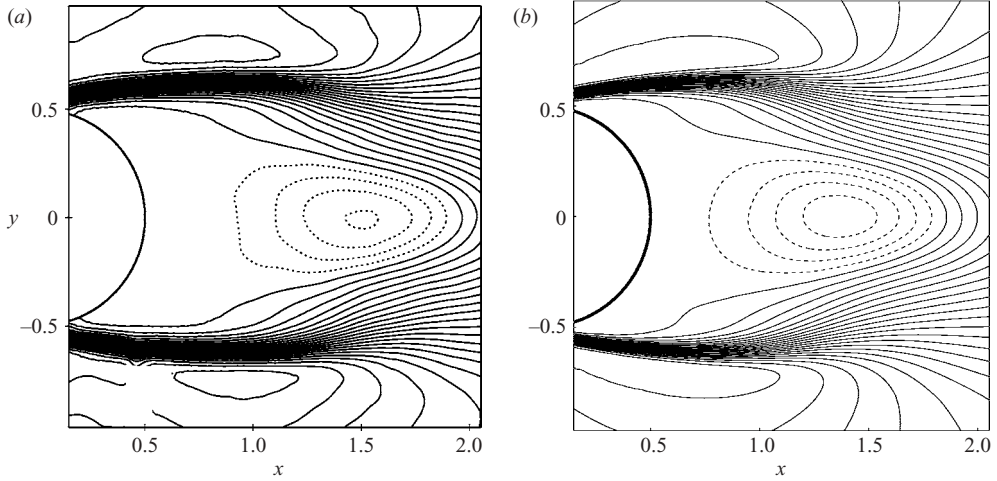


FIGURE 6. Contours of normalized mean streamwise velocity: (a) PIV at $Re = 4000$; (b) DNS at $Re = 3900$. In both plots, $u/U_0|_{min} = -0.252$ and $|\Delta u/U_0| = 0.063$.

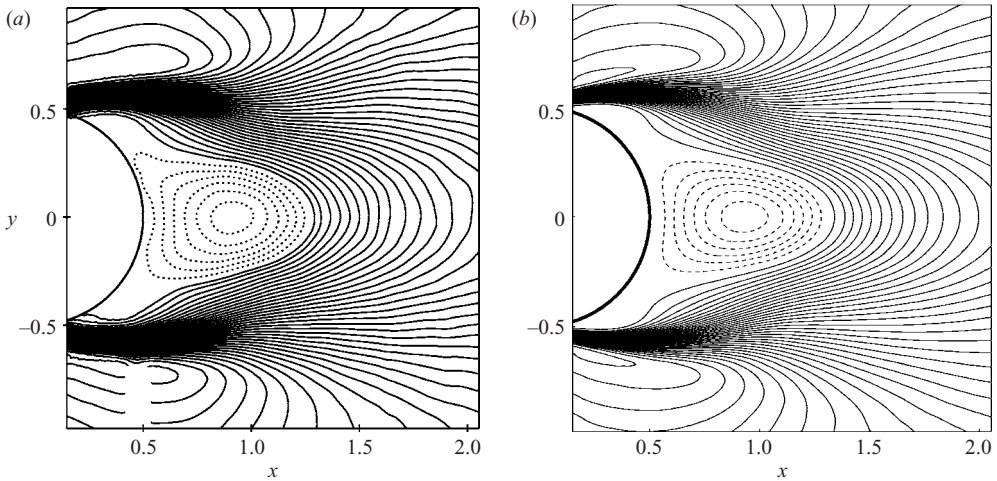


FIGURE 7. Contours of mean streamwise velocity at $Re = 10000$: (a) PIV; (b) DNS. In both plots, $u/U_0|_{min} = -0.228$ and $|\Delta u/U_0| = 0.038$.

velocity on the plane of symmetry are $1.47D$ and $1.36D$, respectively, for experiment and simulation.

Figure 7 shows a corresponding comparison of the normalized mean streamwise velocity μ/U_0 between the experiment (figure 7a) and the simulation (figure 7b) at $Re = 10000$. Consider the region of negative (upstream-oriented) velocity designated by the dashed lines. Both the location and magnitude of the peak value are similar for simulation and experiment. The overall length of the bubble, however, is $0.78D$ and $0.82D$ for experiment and simulation, respectively.

The patterns of normalized streamwise r.m.s. velocity fluctuations u'/U_0 , given in figure 8 for $Re = 4000/3900$, show strong fluctuations in the separating shear layers, and two maxima associated with the vortex formation. The downstream locations

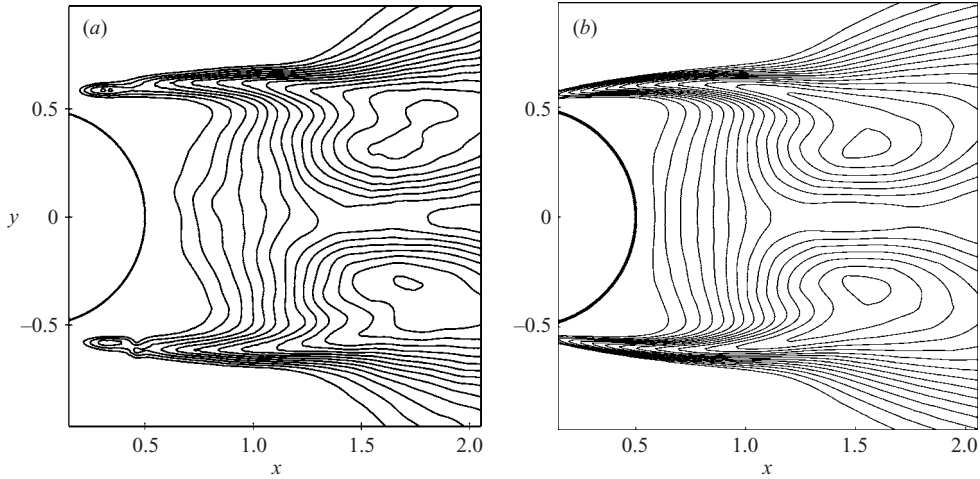


FIGURE 8. Contours of normalized streamwise r.m.s. velocity: (a) PIV at $Re = 4000$; (b) DNS at $Re = 3900$. In both plots, $u'/U_{0|min} = 0.1$ and $\Delta u'/U_0 = 0.025$.

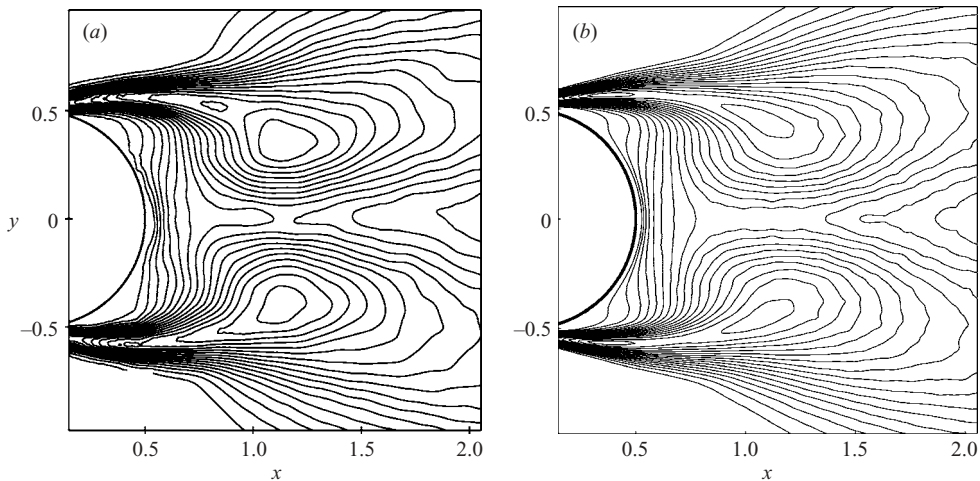


FIGURE 9. Contours of streamwise r.m.s. velocity at $Re = 10000$: (a) PIV; (b) DNS. In both plots, $u'/U_{0|min} = 0.1$ and $\Delta u'/U_0 = 0.025$.

of the r.m.s. maxima are at approximately $x/D = 1.55$ for simulation and 1.72 for experiment, and the respective peak values are 0.45 and 0.425.

Comparison of the normalized streamwise r.m.s. velocity fluctuation u'/U_0 at $Re = 10000$ between the experiment (figure 9a) and the simulation (figure 9b) is shown. While the overall form of the distribution at $Re = 10000$ is similar to that at the lower Reynolds number, the loci of the r.m.s. maxima have moved upstream to $x/D = 1.13$ and 1.14, respectively, for simulation and experiment, and the respective peak values are the same, $u'/U_0 = 0.5$.

The above comparisons between experiment and simulation for $Re = 3900/4000$ and 10000 have demonstrated a relatively high sensitivity of the statistical features of the cylinder wake to variations in Reynolds number. All data show significant changes when the Reynolds number is increased from 4000 to 10000, as shown by Saelim

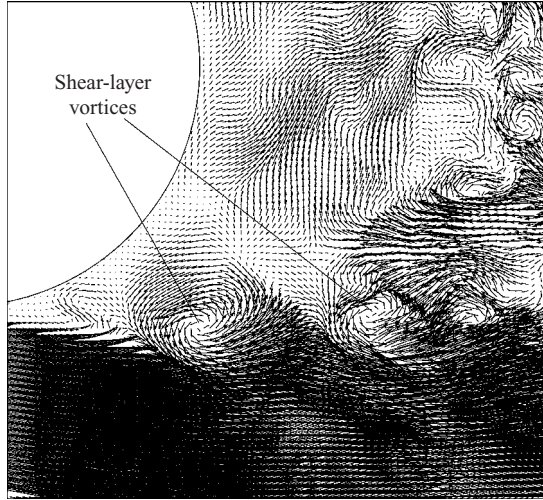


FIGURE 10. Instantaneous velocity vector plot in a two-dimensional (x, y) -plane from DNS showing shear layer vortices at $Re = 3900$.

(2003) and Ekmekci (2006). The reasonably good agreement between experiment and simulation indicates that the simulation accounts well for the essential features of the transition phenomena along the separating shear layers.

4. Shear-layer instability

In the transitional range, the separating shear layers behind the cylinder become unstable, and small-scale vortices can be clearly observed in the shear layers (so-called shear-layer vortices). We next investigate the Reynolds-number effect on the shear-layer instability with DNS data.

Figure 10 shows an instantaneous velocity vector map in a two-dimensional $x - y$ slice of the flow domain at Reynolds number $Re = 3900$. Well-defined vortices are clearly observed in the separating shear-layers with length scales about a quarter of the cylinder diameter. These shear-layer vortices result from the Kelvin–Helmholtz instability and the rolling-up of the cylinder shear layers (Wei & Smith 1986).

Shear-layer vortices are observed to occur at higher frequencies than the Strouhal vortices, in agreement with previous experimental observations. Figure 11(a) shows the time history of the instantaneous crossflow velocity at a point $(x, y, z) = (0.54, 0.65, 2.0)$, which is located in the passage of shear layer vortices in the upper shear layer (note that the line $(x, y) = (0.0, 0.0)$ coincides with the cylinder axis.) In order to reveal the fluctuations, only a time window of 20 convective time units is shown in the plot. Small-scale high-frequency fluctuations caused by the shear-layer vortices are observed to superimpose on top of large-scale fluctuations at the Strouhal frequency. To determine the frequency of shear-layer vortices, we compute the power spectra of the flow velocities in the shear-layer. In figure 11(b), we plot the power spectra of the streamwise and crossflow velocities at the point $x = 0.54$ and $y = 0.65$. The spectrum is averaged over the corresponding points along the homogeneous z -direction. The Strouhal frequency, f_K , and its harmonics are characterized by distinct sharp peaks in the flow spectra. In addition, another peak can be observed, corresponding to the frequency of shear-layer vortices (f_{SL}), at a value significantly higher than the Strouhal frequency. The spectral peak at f_{SL}

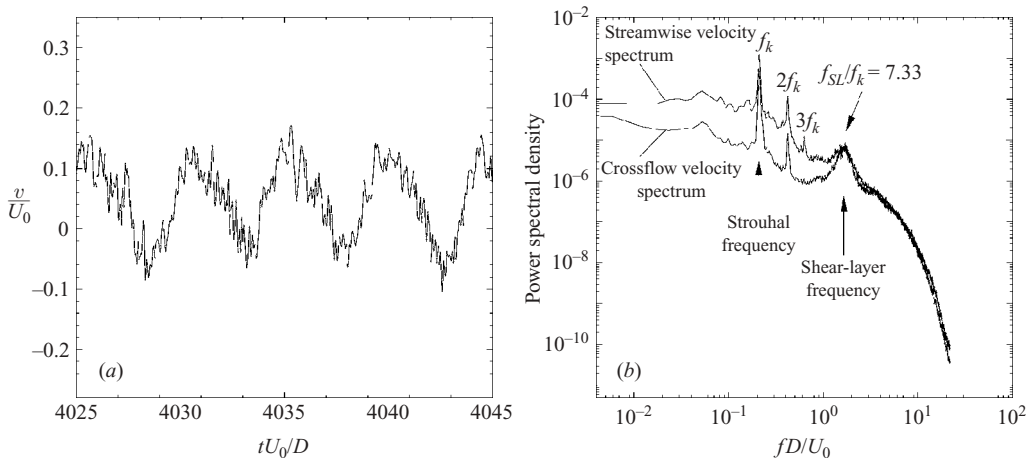


FIGURE 11. Shear-layer instability at $Re = 3900$. Time history of instantaneous crossflow velocity (only a window of 20 convective time units is shown here) (a) and the velocity power spectra (b) at the point $x = 0.54$ and $y = 0.65$ in the shear layer. The power spectrum is obtained by averaging points along the spanwise direction.

appears to be broad, in contrast to the sharp peak at the Strouhal frequency and its harmonics. The broadband peak at f_{SL} indicates that the shear-layer vortices occur in a range of frequencies. These characteristics are consistent with previous experimental observations (Prasad & Williamson 1997; Cardell 1993; Norber 1987). Prasad & Williamson (1997) suggest that temporal variations in the velocity scale owing to the Kármán vortex formation and in the momentum thickness of the shear layer caused by the oscillation of the point of separation, contribute to the variation in time of the most unstable frequency, and thus to the broadband nature of the frequency of shear-layer vortices.

The high-frequency shear-layer vortices appear to be confined to the very near wake of the cylinder. The broadband peak which is characteristic of the flow spectra in the shear layers vanishes downstream of the shear layer. This is evident from figure 12, in which we plot the streamwise and crossflow velocity spectra at a point downstream of the shear layer ($x = 3.14$ and $y = 0.4$) at $Re = 3900$.

Most observations about the shear layer vortices at $Re = 3900$ can be extended to the higher Reynolds number $Re = 10\,000$. In figure 13, we plot the velocity vectors in a two-dimensional $x - y$ slice of the flow domain to visualize the shear-layer vortices at $Re = 10\,000$. Well-defined vortices with length scales about a tenth of the cylinder diameter are evident in the shear layers. Compared to $Re = 3900$, these shear-layer vortices are discernible in regions more upstream at $Re = 10\,000$, indicating that the point of transition moves upstream as the Reynolds number increases.

The characteristics of shear-layer velocities at $Re = 10\,000$ are demonstrated in figure 14(a), in which we plot the time trace of the crossflow velocity at the point $(x, y, z) = (0.42, 0.55, 2.3)$ in the passage of shear-layer vortices. Only a time window of 20 convective time units is shown in the plot for clarity. High-frequency fluctuations caused by shear-layer vortices dominate the cross-flow velocity with substantially larger fluctuation amplitudes at $Re = 10\,000$, while the fluctuations at the Strouhal frequency caused by the Kármán vortex formation are overwhelmed and hardly discernible, unlike $Re = 3900$ (see figure 11a). The power spectrum of the crossflow velocity at the point $x = 0.42$ and $y = 0.55$ is shown in figure 14(b). The Strouhal

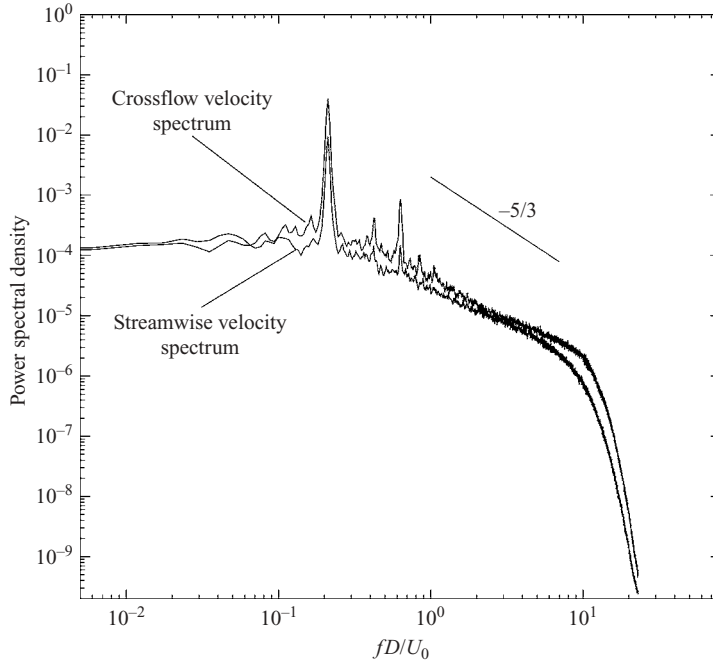


FIGURE 12. Flow spectra downstream of shear layer at $Re = 3900$. Streamwise and crossflow velocity spectra at the point $x = 3.14$ and $y = 0.40$.

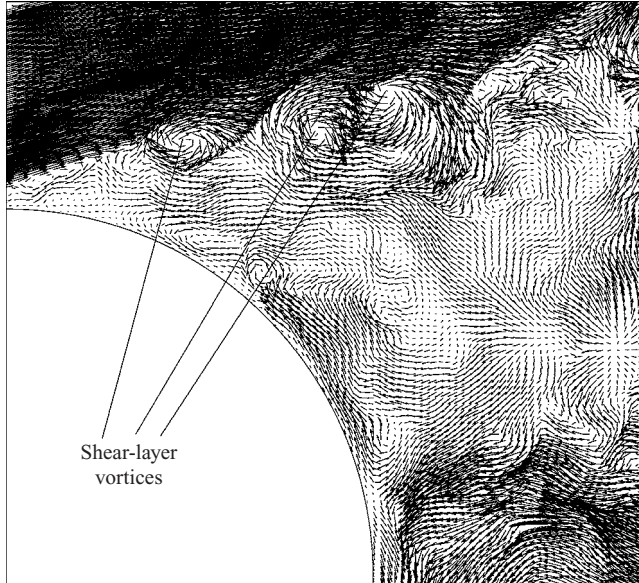


FIGURE 13. Instantaneous velocity vector plot in a two-dimensional (x, y) -plane from DNS showing shear layer vortices at $Re = 10000$.

frequency f_K has a sharp spectral peak, similar to that at $Re = 3900$. A notable feature of the spectrum, however, is that no well-defined spectral peak is observed at the shear-layer vortex frequency. Rather, the shear-layer vortices are signified by a high spectral-density ‘plateau’ in the spectrum at frequencies ranging from $f_{SL}^L/f_K = 7.83$ to

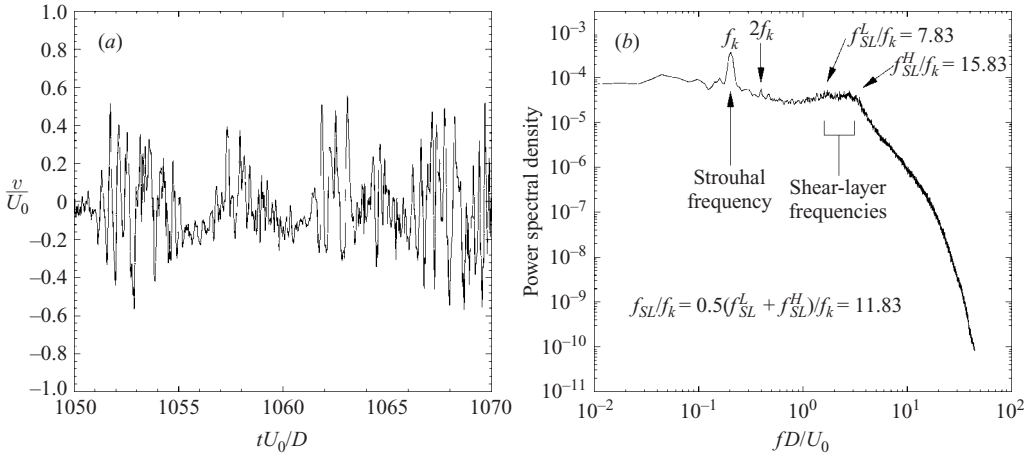


FIGURE 14. Shear-layer instability at $Re=10\,000$. Time history of instantaneous crossflow velocity (only a window of 20 convective time units is shown here) (a) and the power spectra of crossflow velocity (b) at point $x=0.42$ and $y=0.55$ in the shear layer.

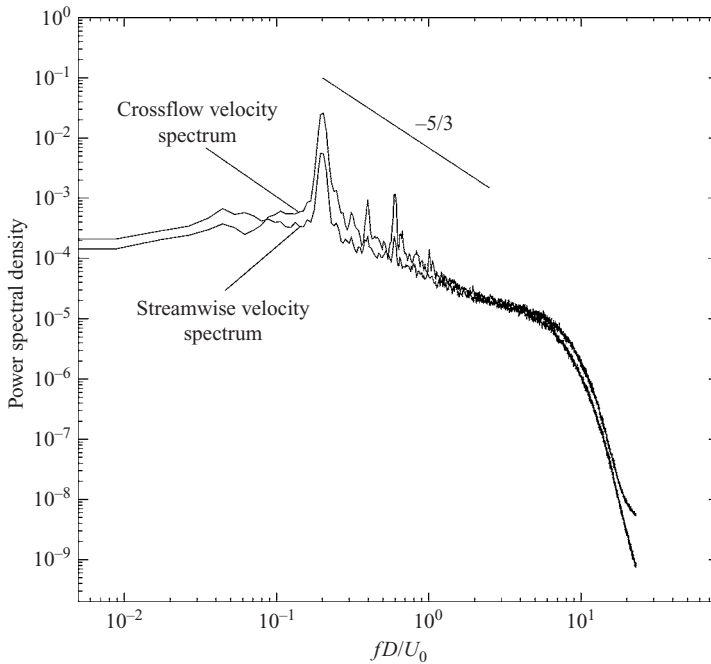


FIGURE 15. Flow spectra downstream of shear layer at $Re=10\,000$. Streamwise and crossflow velocity spectra at the point $x=3.01$ and $y=0.38$.

$f_{SL}^H/f_k = 15.83$, with essentially constant spectral density in this range. This indicates that the shear-layer vortices are characterized by a band of frequencies at $Re=10\,000$, ranging from 7.83 to 15.83 when normalized by the Strouhal frequency. Figure 15 shows the power spectra of streamwise and crossflow velocities at a point downstream of the shear layer. The disappearance of the shear-layer vortex signature in the spectra is indicative of the spatial locality of these vortices.

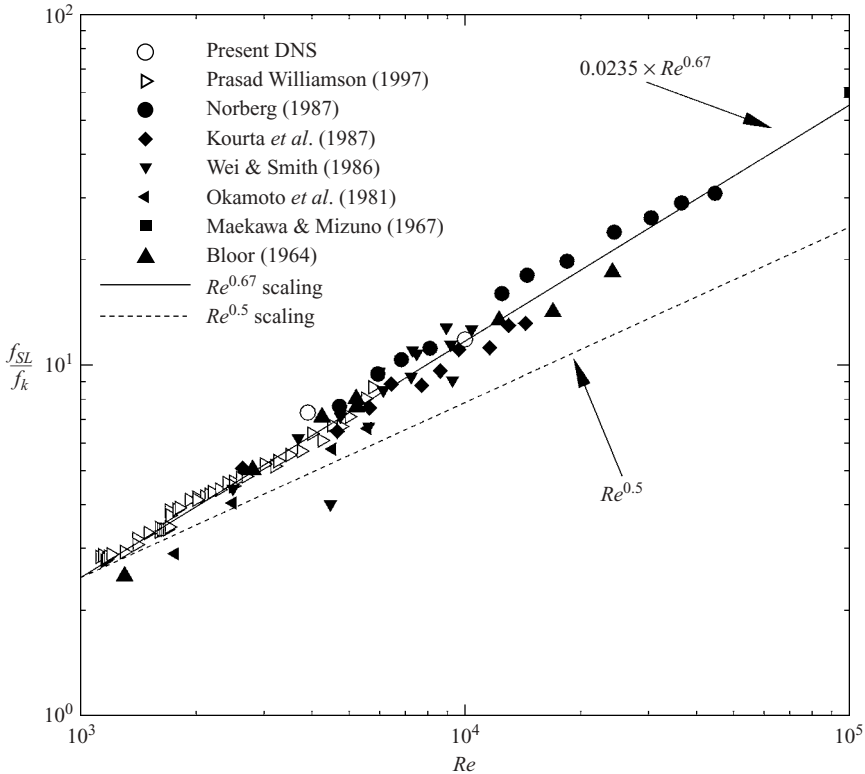


FIGURE 16. Variation of shear-layer frequency with Reynolds number. The plot includes data from present DNS and previous experimental investigations. All the experimental data points are courtesy of C. H. K. Williamson.

In figure 16, we plot the shear-layer frequencies from current simulations for Reynolds numbers $Re = 3900$ and 10000 , and from previous experimental measurements as a function of Reynolds number. We have used the mean value of the shear-layer frequencies, $f_{SL} = (f_{SL}^L + f_{SL}^H)/2 = 11.83$, in the plot for $Re = 10000$. The power-law scaling relations suggested by Prasad & Williamson (1997) and by Bloor (1964) are also shown in the plot as solid and dashed lines, respectively. Evidently, the shear-layer frequencies from the present DNS agree well with experimentally measured values, and the results seem to support the $Re^{0.67}$ power law suggested by Prasad & Williamson (1997). Using the shear-layer frequency data of Norberg (1987) and Prasad & Williamson (1997), Thompson & Hourigan (2005) provide a detailed assessment and model of the variation of f_{SL} over the range of Reynolds number $Re = 1500$ to 50000 , with a scaling exponent 0.57 for $Re < 5000$ and 0.52 for $Re > 10000$. Rajagopalan & Antonia (2005) show a scaling exponent of 0.65 , basically in agreement with Prasad & Williamson's (1997) power law.

5. Concluding remarks

In this paper, we have investigated the effects of Reynolds number on the statistical characteristics of the cylinder wake and on the shear-layer instability in the transitional range. By combining PIV measurements and direct-numerical simulations at Reynolds numbers $Re = 3900/4000$ and 10000 , we observe that the flow statistics such as the

mean velocity and vorticity, Reynolds stress, and r.m.s. fluctuations are notably altered with the variation of Reynolds number. A general observation is that the principal features of all quantitative patterns move upstream with increasing value of Reynolds number. Patterns of mean (time-averaged) streamwise velocity indicate that the bubble enclosing the region of negative velocity in the near-wake region becomes significantly smaller, i.e. the location of zero velocity along the plane of symmetry of the bubble moves upstream with increasing Reynolds number. Furthermore, corresponding patterns of mean spanwise vorticity, fluctuating velocity field, extrema of streamwise velocity and Reynolds stress all contract towards the base of the cylinder with increasing Reynolds number. The patterns of Reynolds stress show extensions along the edge of the separated shear layer towards the separation point at higher values of Reynolds number, i.e. increased levels of Reynolds stress occur further upstream along the separating layer, which suggests earlier onset of transition.

The variation of Reynolds number also influences the shear-layer instability significantly. At $Re = 3900$, simulations indicate that the shear-layer velocity is characterized by high-frequency low-amplitude fluctuations caused by shear-layer vortices superimposed on top of large-scale fluctuations caused by Kármán vortex formation at the Strouhal frequency. As the Reynolds number increases to 10 000, the high-frequency fluctuations caused by shear-layer vortices are observed to dominate the shear-layer velocity and overwhelm the fluctuations caused by Kármán vortex formation. Shear-layer vortices imprint a signature onto the flow spectra. At $Re = 3900$ the shear-layer velocity spectra exhibit a broadband peak at the shear-layer frequency, in contrast to the distinct sharp peak at the Strouhal frequency. As the Reynolds number increases to 10 000, the shear-layer vortices are signified by a broadband ‘plateau’ in the spectrum with constant high spectral density, and no clear spectral peak is observed. The signatures of shear-layer vortices vanish from the spectrum downstream of the shear layer. Comparison with previous measurements indicates that shear-layer frequencies from the current study agree well with experimentally measured values and follow the $Re^{0.67}$ power law suggested by Prasad & Williamson (1997).

Appendix A. DNS resolution studies at $Re = 10\,000$

Consider the three-dimensional incompressible turbulent flow past a circular cylinder. Figure 17 shows a ‘z-slice’ of the computational mesh. We conducted simulations on two spectral element meshes in (x, y) -planes: a coarser mesh consisting of $K = 6272$ triangular elements (figure 17*a*) and a mesh significantly refined around and in the near wake of the cylinder that consists of $K = 9272$ triangular elements (figure 17*b*). The order of expansion polynomials on each element is varied between $P = 4$ and $P = 5$. Figure 17(*c*) shows the mean streamwise velocity profile along a vertical line crossing the cylinder axis. It indicates that within the cylinder boundary layer we have over one layer of spectral elements (or more than 7 grid points) with the coarser mesh (figure 17*a*), and over two layers of spectral elements (or more than 14 grid points) with the finer mesh (figure 17*b*).

Simulations were performed with different grid resolutions by varying the number of grid points (or Fourier modes) in the spanwise direction and the order of spectral elements in the (x, y) -planes on the two meshes. Table 2 summarizes the values of several physical quantities under a number of resolutions from the simulation together with their experimental values at $Re = 10\,000$. The drag coefficients, base

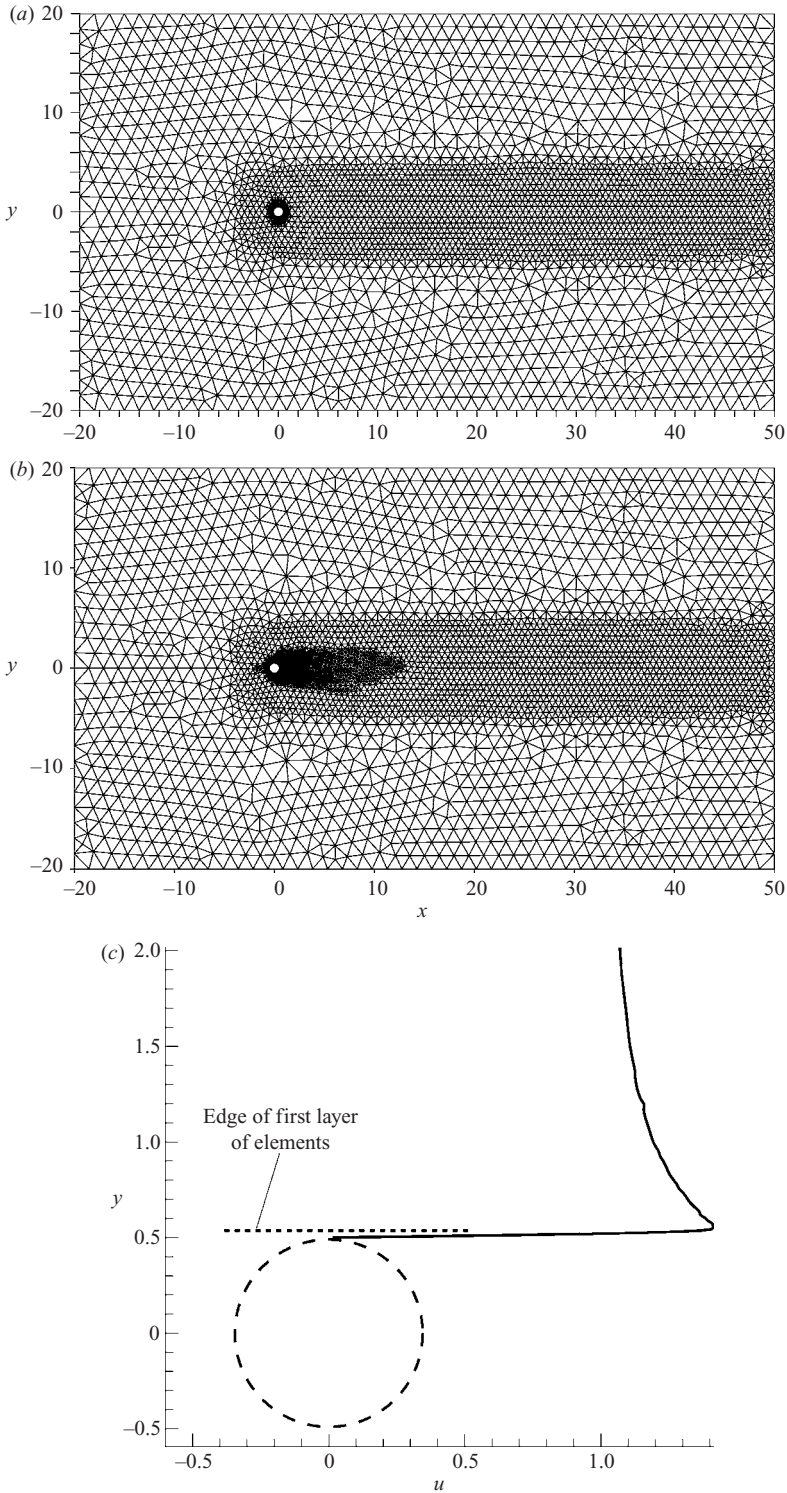


FIGURE 17. Two-dimensional slice of mesh in (x, y) -planes and resolutions for $Re = 10000$ simulations: (a) low-resolution mesh consisting of 6272 triangular spectral elements; (b) high-resolution mesh consisting of 9272 triangular spectral elements; (c) mean streamwise velocity profile along a vertical line crossing the cylinder axis.

	C_d	$-C_{p_b}$	St	C_L
DNS ($P = 5$, $N_z = 16$, $K = 6272$)	1.155	1.129	0.195	0.538
DNS ($P = 5$, $N_z = 64$, $K = 6272$)	1.110	1.084	0.209	0.565
DNS ($P = 5$, $N_z = 128$, $K = 6272$)	1.128	1.171	0.205	0.574
DNS ($P = 5$, $N_z = 32$, $K = 9272$)	1.208	1.201	0.200	0.547
DNS ($P = 4$, $N_z = 64$, $K = 9272$)	1.120	1.056	0.205	0.497
DNS ($P = 5$, $N_z = 128$, $K = 9272$)	1.143	1.129	0.203	0.448
Wieselsberger (1921)	1.104	–	–	–
Bishop & Hassan (1964)	–	–	0.201	0.463
Norberg (1987)	–	1.112	0.201	–
Moeller & Leehey (1984)	–	–	–	0.532
Gopalkrishnan (1993)	1.186	–	0.193	0.384
West & Apelt (1993)	–	–	–	0.461
Norberg (2003)	–	–	0.202	0.394

TABLE 2. Physical quantities in the flow past a circular cylinder at $Re = 10\,000$: drag coefficient C_d , base pressure coefficient C_{p_b} , Strouhal number St , and r.m.s. lift coefficient C_L . The order of spectral elements is denoted by P . See the caption of table 1 for the meanings of the other symbols.

pressure (suction) coefficients, and the Strouhal number from the simulation agree with the experimental data reasonably well for all resolutions, indicating that these physical quantities are generally not quite sensitive to the grid resolution. On the other hand, the lift coefficient (based on r.m.s. lift) demonstrates a higher sensitivity to the resolution. With the low-resolution mesh, the lift coefficient values from the simulation generally lie at the upper bound of the range of experimental lift coefficient data, and the value increases slightly as the number of Fourier modes in the spanwise direction increases. With the high-resolution mesh, the lift coefficient values decrease as the number of Fourier modes in the spanwise direction increases, and lie within the range of the experimental values. It is noted that the lift coefficient demonstrates a wide spread in the experiments as well. For example, Gopalkrishnan (1993) observes that the lift coefficient varies between 0.3 and 0.5 from one experimental run to another. This is also evident from the scatter of the experimental lift coefficient values in table 2.

Figure 18 shows a window of the time history of the drag and lift coefficients for the case $P = 5$, $N_z = 128$ and $K = 9272$. The time traces reveal the quasi-periodic behaviour of drag and lift coefficients, with their amplitudes varying irregularly over time. Figure 19 shows the mean pressure coefficient on the cylinder surface as a function of the angle, with the zero degree angle located at the front stagnation point. The figure shows the results on both the low- and high-resolution meshes at $Re = 10\,000$ from the simulation, together with the experimental data by Norberg (1993) at $Re = 8000$. The low-resolution mesh captures the pressure on the front and back portions of the cylinder surface reasonably well. However, it over-predicts the magnitude of the minimum pressure on the cylinder surface and the angle at which the minimum occurs. The results from the high-resolution mesh, on the other hand, agree with the experimental data quite well on the entire cylinder surface.

Appendix B. Additional case studies on DNS spanwise resolution at $Re = 3900$

To complement the resolution study in Ma *et al.* (2000) at $Re = 3900$, especially on the effect of spanwise resolution, we have carried out additional simulations and

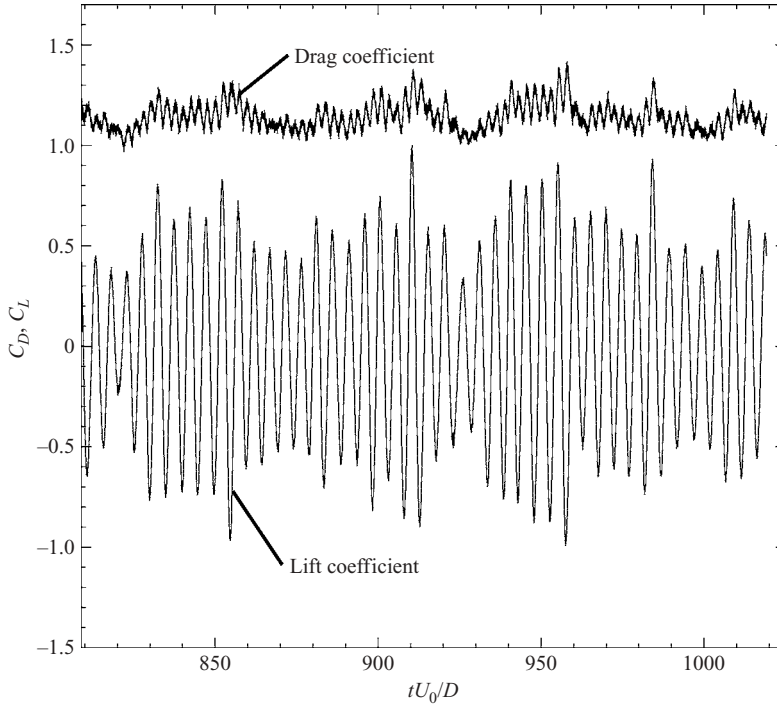


FIGURE 18. Time history of drag and lift coefficients of flow past a circular cylinder at $Re = 10000$ (on high-resolution mesh).

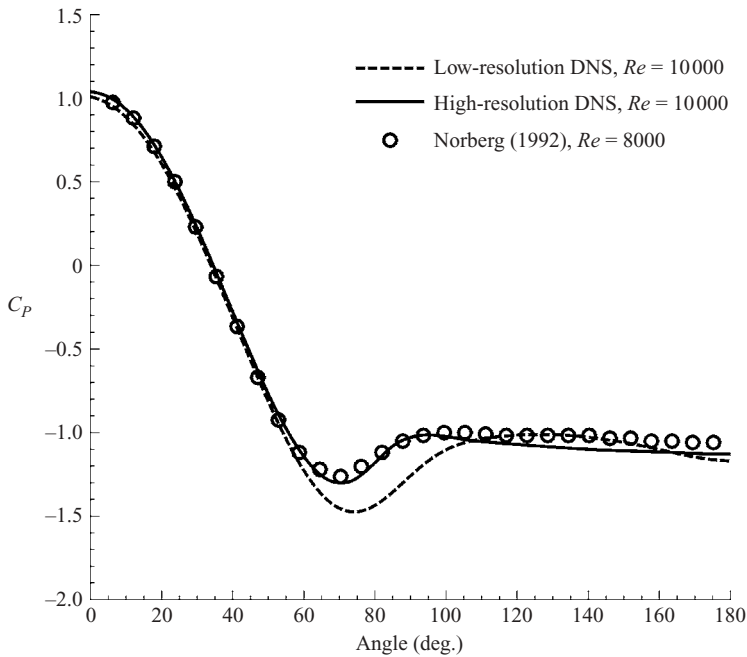


FIGURE 19. Comparison of pressure coefficient on cylinder surface between simulation ($Re = 10000$) and experimental data ($Re = 8000$) in Norberg (1993).

Case	P	K	N_z	L_z/D	$-C_{pb}$	St	Bubble length/ D
A	8	902	64	1.5π	1.04	0.206	1.00
B	8	902	128	1.5π	0.96	0.210	1.12
C	8	902	192	1.5π	0.93	0.208	1.18
I	10	902	256	2π	0.96	0.203	1.12

TABLE 3. Additional case studies on spanwise resolution at $Re = 3900$ in DNS. For the meanings of symbols see the captions of tables 1 and 2. (Case I is taken from Ma *et al.* 2000).

summarized the results in table 3. Cases A, B and C in the table are the current simulations while Case I is taken from Ma *et al.* (2000), the highest resolution in that paper, as the reference case. These additional results are computed on a domain with a spanwise dimension 1.5π (normalized by the cylinder diameter), with the 902-element mesh and an element order 8. Spanwise resolutions are varied by changing the number of Fourier modes in the z -direction, ranging from 32 (or 64 grid points) to 96 (or 192 grid points) for different cases in table 3. The variation in Strouhal number is within 2% for different spanwise resolutions. The base suction coefficient decreases and the bubble length increases to a certain degree with increasing spanwise resolution. The differences of these global parameters between Case C (highest spanwise resolution considered here) and the reference Case I range from about 2% to 5%.

The work of both groups was supported by ONR (Dr Thomas F. Swain). Computer time was provided by DOD HPCMP (ARSC, NAVO, ERDC, ARL) and NSF PSC/NCSA. We would like to thank Professor C. H. K. Williamson for providing the shear-layer frequency experimental data.

REFERENCES

- BATCHO, P. & KARNIADAKIS, G. E. 1991 Chaotic transport in two- and three-dimensional flow past a cylinder. *Phys. Fluids A* **3**, 1051–1062.
- BEAUDAN, P. & MOIN, P. 1994 Numerical experiments on the flow past a circular cylinder at subcritical Reynolds number. Report TF-62, Department of Mechanical Engineering, Stanford University.
- BISHOP, R. E. D. & HASSAN, A. Y. 1964 The lift and drag forces on a circular cylinder in a flowing fluid. *Proc. R. Soc. Lond. A* **277**, 32–50.
- BLOOR, M. S. 1964 The transition to turbulence in the wake of a circular cylinder. *J. Fluid Mech.* **19**, 290–304.
- BRAZA, M., CHAISSAING, P. & HA MINH, H. 1990 Prediction of large-scale transition features in the wake of a circular cylinder. *Phys. Fluids A* **2**, 1461–1521.
- BREDE, M. 2004 Measurement of turbulence production in the cylinder separated shear-layer using event-triggered laser-Doppler anemometry. *Exps. Fluids* **36**, 860–866.
- BREUER, M. 1998 Numerical and modeling influences on large eddy simulations for the flow past a circular cylinder. *Intl J. Heat Fluid Flow* **19**, 512–521.
- BREUER, M. 2000 A challenging test case for large eddy simulation: high Reynolds number circular cylinder flow. *Intl J. Heat Fluid Flow* **21**, 648–654.
- CARDELL, G. S. 1993 Flow past a circular cylinder with a permeable wake splitter plate. PhD thesis, Graduate Aeronautical Laboratory, California Institute of Technology.
- CHYU, C.-K. & ROCKWELL, D. 1996 Near-wake structure of an oscillating cylinder: effect of controlled shear-layer vortices. *J. Fluid Mech.* **322**, 21–49.
- EKMEKCI, A. 2006 Control of the near-wake of a circular cylinder: effects of surface, disturbances. Ph.D. Dissertation, Department of Mechanical Engineering and Mechanics, Lehigh University, Bethlehem, PA.

- FRANKE, J. & FRANK, W. 2002 Large eddy simulation of the flow past a circular cylinder at $Re = 3900$. *J. Wind Engng Indust. Aerodyn.* **90**, 1191–1206.
- FILLER, J. R., MARSTON, P. L. & MIH, W. C. 1991 Response of the shear layers separating from a circular cylinder to small-amplitude rotational oscillations. *J. Fluid Mech.* **31**, 481–499.
- FU, H. & ROCKWELL, D. 2005 Shallow flow past a cylinder: transition phenomena at low Reynolds number. *J. Fluid Mech.* **540**, 75–97.
- GERRARD, J. H. 1967 Experimental investigation of separated boundary layer undergoing transition to turbulence. *Phys. Fluids* **10**, S98–100.
- GERRARD, J. H. 1978 The wakes of cylindrical bluff bodies at low Reynolds number. *Phil. Trans. R. Soc. Lond. A* **288**, 351–382.
- GOPALKRISHNAN, R. 1993 Vortex-induced forces on oscillating bluff cylinders. PhD thesis, Department of Ocean Engineering, MIT, Cambridge, MA, USA.
- JORDAN, S. A. 2002 Investigation of the cylinder separated shear-layer physics by large-eddy simulation. *Intl J. Heat Fluid Flow* **23**, 1–12.
- JORDAN, S. A. 2003 Resolving turbulent wakes. *J. Fluids Engng* **125**, 823–834.
- KALRO, V. & TEZDUYAR, T. 1997 Parallel 3D computation of unsteady flows around circular cylinders. *Parallel Comput.* **23**, 1235–1248.
- KARNIADAKIS, G. E., ISRAELI, M. & ORSZAG, S. A. 1991 High-order splitting methods for the incompressible Navier–Stokes equations. *J. Comput. Phys.* **97**, 414–443.
- KARNIADAKIS, G. E. & SHERWIN, S. J. 2005 *Spectral/hp Element Methods for CFD*, 2nd edn. Oxford University Press.
- KOURTA, A., BOISSON, H. C., CHASSAING, P. & HA MINH, H. 1987 Nonlinear interaction and the transition to turbulence in the wake of a circular cylinder. *J. Fluid Mech.* **181**, 141–161.
- KRAVCHENKO, A. G. & MOIN, P. 2000 Numerical studies of flow over a circular cylinder at $Re_D = 3900$. *Phys. Fluids* **12**, 403–417.
- LIN, J.-C., TOWFIGHI, J. & ROCKWELL, D. 1995 Instantaneous structure of near-wake of a cylinder: on the effect of Reynolds number. *J. Fluids Struct.* **9**, 409–418.
- LINKE, W. 1931 Neue messungen zur aerodynamik des zylinders, insbesondere seines reinen reibungswiderstandes. *Phys. Z.* **32**, 900–914.
- MA, X., KARAMANOS, G.-S. & KARNIADAKIS, G. E. 2000 Dynamics and low-dimensionality of a turbulent near wake. *J. Fluid Mech.* **410**, 29–65.
- MCCROSKEY, W. J. 1977 Some current research in unsteady fluid dynamics – the 1976 Freeman scholar lecture. *J. Fluids Engng* **99**, 8–39.
- MITTAL, R. & BALACHANDAR, S. 1995 Effect of three-dimensionality on the lift and drag of nominally two-dimensional cylinders. *Phys. Fluids* **7**, 1841–1865.
- MITTAL, R. & MOIN, P. 1997 Suitability of upwind-biased finite-difference schemes for large-eddy simulation of turbulent flows. *AIAA J.* **35**, 1415–1417.
- MITTAL, S. & KUMAR, V. 2001 Flow-induced vibrations of a light circular cylinder at Reynolds numbers 10^3 to 10^4 . *J. Sound Vib.* **245**, 923–946.
- MOELLER, M. J. & LEEHEY, P. 1984 Unsteady forces on a cylinder in cross flow at subcritical Reynolds numbers. In *ASME Symposium on Flow-induced Vibrations* (ed. M. P. Paidoussis, O. M. Griffin & M. Sevik), New Orleans, ASME, New York, vol. 1, pp. 57–71.
- NOCA, F., PARK, H. G. & GHARIB, M. 1998 Vortex formation length of a circular cylinder ($300 < Re < 4000$) using DPIV. *Proc. Bluff Body Wakes and Vortex-Induced Vibration* (ed. P. W. Bearman & C. H. K. Williamson), Washington, DC, June, Paper 46. Also ASME, FEDSM 98-5149.
- NORBERG, C. 1987 Effect of Reynolds number and a low-intensity freestream turbulence on the flow around a circular cylinder. *Publ. 87/2*. Department of Applied thermodynamics and Fluid Mechanics, Chalmers University of Technology.
- NORBERG, C. 1993 Pressure forces on a circular cylinder in cross flow. In *Bluff Body Wakes, Dynamics and Instabilities* (ed. H. Eckelmann, J. M. Graham, P. Huerre & P. A. Monkewitz), *Proc. IUTAM Symp. 115*, 7–11 September 1992, Göttingen. Springer.
- NORBERG, C. 1994 An experimental investigation of the flow around a circular cylinder: influence of aspect ratio. *J. Fluid Mech.* **258**, 287–316.
- NORBERG, C. 1998 LDV measurements in the near-wake of a circular cylinder. *Proc. Bluff Body Wakes and Vortex-Induced Vibration* (ed. P. W. Bearman & C. H. K. Williamson), Washington, DC, June, Paper 42. Also ASME, FEDSM 98-5202.

- NORBERG, C. 2003 Fluctuating lift on a circular cylinder: review and new measurements. *J. Fluids Struct.* **17**, 57–96.
- PRASAD, A. & WILLIAMSON, C. H. K. 1997 The instability of the shear layer separating from a bluff body. *J. Fluid Mech.* **333**, 375–402.
- RAJAGOPALAN, S. & ANTONIA, R. A. 2005 Flow around a circular cylinder – structure of the near wake shear layer. *Exps Fluids* **38**, 393–402.
- ROSHKO, A. 1993 Perspectives on bluff-body aerodynamics. *J. Wind Engng Indust. Aerodyn.* **49**, 79–100.
- ROSHKO, A. & FISZDON, W. 1969 On the persistence of transition in the near-wake. *Problems of Hydrodynamics and Continuum Mechanics*, pp. 606–616. SIAM.
- SAELIM, N. 2003 Flow past a cylinder: effect of surface modification on structure of the near-wake. PhD dissertation, Department of Mechanical Engineering and Mechanics, Lehigh University, Bethlehem, PA.
- SHERIDAN, J., SORIA, J., WU, J. & WELSH, W. C. 1993 The Kelvin–Helmholtz instability of the separated shear layer from a circular cylinder. In *Bluff Body Wakes, Dynamics and Instabilities* (ed. H. Eckelmann, J. M. Graham, P. Huerre and P. A. Monkewitz), *Proc. IUTAM Symp.* 115, 7–11 September 1992, Göttingen. Springer.
- SZEPESY, S. & BEARMAN, P. W. 1992 Aspect ratio and end plate effects on vortex shedding from a circular cylinder. *J. Fluid Mech.* **234**, 191–217.
- THOMPSON, M. C. & HOURIGAN, K. 2005 The shear-layer instability of a circular cylinder wake. *Phys. Fluids* **17**, 021702.
- UNAL, M. F. & ROCKWELL, D. 1988 On vortex formation from a cylinder. Part 1. The initial instability. *J. Fluid Mech.* **190**, 491–512.
- WEI, T. & SMITH, C. R. 1986 Secondary vortices in the wake of circular cylinders. *J. Fluid Mech.* **169**, 513–533.
- WEST, G. S. & APELT, C. J. 1993 Measurements of fluctuating pressures and forces on circular cylinder in the Reynolds number range 10^4 to 2.5×10^5 . *J. Fluids Struct.* **7**, 227–244.
- WIESELSBERGER, C. 1921 Neuere Feststellungen über die Gesetze des Flüssigkeits- und Luftwiderstandes. *Phys. Z.* **22**, 321–328.
- WILLIAMSON, C. H. K. 1996 Vortex dynamics in a cylinder wake. *Annu. Rev. Fluid Mech.* **28**, 477–539.
- ZDRAVKOVICH, M. M. 1990 Conceptual overview of laminar and turbulent flows past smooth and rough circular cylinders. *J. Wind Engng Indust. Aero.* **33**, 53–62.